



Quantitative characterization of zebrafish development based on multiple classifications using Mueller matrix OCT

KE LI,^{1,†} BIN LIU,^{1,†} ZAIFAN WANG,¹ YAO LI,¹ HUI LI,¹ SHULIAN WU,^{1,3}  AND ZHIFANG LI^{1,2,4} 

¹Key Laboratory of Optoelectronic Science and Technology for Medicine, Ministry of Education, Fujian Provincial Key Laboratory of Photonics Technology, Fujian Provincial Engineering Technology Research Center of Photoelectric Sensing Application, College of Photonic and Electronic Engineering, Fujian Normal University, Fuzhou, Fujian, 350007, China

²Bionovel Lab, Guangzhou, Guangdong, 510407, China

³slwu@fjnu.edu.cn

⁴lizhifang@fjnu.edu.cn

[†]These authors contributed equally to this work

Abstract: Organ development analysis plays an important role in assessing an individual's growth health. In this study, we present a non-invasive method for the quantitative characterization of zebrafish multiple organs during their growth, utilizing Mueller matrix optical coherence tomography (Mueller matrix OCT) in combination with deep learning. Firstly, Mueller matrix OCT was employed to acquire 3D images of zebrafish during development. Subsequently, a deep learning based U-Net network was applied to segment various anatomical structures, including the body, eyes, spine, yolk sac, and swim bladder of the zebrafish. Following segmentation, the volume of each organ was calculated. Finally, the development and proportional trends of zebrafish embryos and organs from day 1 to day 19 were quantitatively analyzed. The obtained quantitative results revealed that the volume development of the fish body and individual organs exhibited a steady growth trend. Additionally, smaller organs, such as the spine and swim bladder, were successfully quantified during the growth process. Our findings demonstrate that the combination of Mueller matrix OCT and deep learning effectively quantify the development of various organs throughout zebrafish embryonic development. This approach offers a more intuitive and efficient monitoring method for clinical medicine and developmental biology studies.

© 2023 Optica Publishing Group under the terms of the [Optica Open Access Publishing Agreement](#)

1. Introduction

Numerous factors influence the growth and development of humans and animals, leading to varying developmental states during embryonic development. Insufficient nutrition, poor living conditions, and heredity can contribute to developmental delays, deformities, and even multiple organ failure in severe cases [1,2]. Therefore, early diagnosis of embryonic development is essential for both human and animal health.

In recent decades, zebrafish has been widely used as a research model for organ and embryo development due to their small size, transparent embryos, ease of in vitro fertilization observation, and strong reproductive capacity [3]. Furthermore, zebrafish and humans share up to 70% gene homology [4], making zebrafish an invaluable experimental model for studying developmental biology, embryogenesis, pathology, and developmental regeneration [5,6]. Riddle et al. summarized the use of zebrafish as a model to study the influence of nutrition on embryonic structural development and emphasized their potential in investigating developmental nutrition control [7]. Han et al. employed zebrafish to investigate the effects of precise folic acid supplementation doses on embryonic and heart development, concluding that both insufficient and excessive folic

acid levels could lead to developmental abnormalities such as ventricular pericardial edema or abnormal cardiac circulation [8]. Huang et al. recognized the advantages of zebrafish in studying craniofacial bone development due to their simple craniofacial structure, transparent embryos, and ease of observing facial morphogenesis [9]. This makes zebrafish a valuable model for identifying environmental factors related to craniofacial skeletal malformation etiology. Qian et al. showed that phthalates can cause spinal defects in zebrafish embryos [10]. Collectively, these studies illustrate the widespread application of zebrafish in examining the impact of environmental factors or nutritional intake on embryonic development. Both internal and external factors can cause organ malformations, so it is necessary to accurately confirm organ structure in the study of abnormal development of embryos and larvae. To provide a more precise diagnosis of organ development, detailed segmentation of organs during growth is required. This analysis will reveal vital information about the shape and volume changes of different organs throughout development [11,12].

Currently, a variety of imaging techniques have been employed for studying zebrafish and its' image segmentation, including computed tomography (CT) [13], positron emission tomography (PET) [14], confocal microscopy [15], and fluorescence microscopy [16]. However, each method presents its own set of limitations. CT involves exposure to high doses of harmful radiation. PET, despite its widespread clinical use due to high tissue sensitivity and specificity, suffers from low spatial resolution and accuracy. Additionally, PET imaging necessitates the use of a contrast agent, making it difficult to diagnose many diseases [11,12,17,18]. Light and fluorescence microscopy techniques are considered as standard imaging methods in zebrafish studies [19,20]. These methods are particularly effective for imaging zebrafish embryos and larvae up to approximately 5 days post-fertilization (dpf) to 7 dpf. The efficacy of these techniques is primarily due to their ability to capture high-resolution images of external morphological features, as well as facilitating the investigation of interactions between different cell types during zebrafish development. However, as the zebrafish matures and transitions into more advanced developmental stages, such as the adult stage, the use of light and fluorescence microscopy decreases, owing to the increased complexity and size of the organism, and the inherent challenges associated with visualizing internal organs and tissues. In addition, fluorescence microscopy enables *in vivo* observation of dynamic samples but requires a fluorescent dye [21]. Optical Coherence Tomography (OCT) represents a non-invasive imaging technique that overcomes the limitations of other imaging techniques, proving particularly useful for the imaging of adult zebrafish in longitudinal studies focused on disease progression or drug response evaluation.

OCT is a biomedical imaging technology for subsurface tissue imaging with high resolution (less than ten micrometers) and a penetration depth of several millimeters [22]. OCT relies on the optical scattering properties of tissues, which exhibit contrast with biological structure and phase information [23]. With its high-speed imaging, high signal-to-noise ratio, and non-invasive nature, OCT has been found widespread application in biomedical research. OCT imaging is similar to ultrasound B-mode imaging, except that it measures the echo delay and intensity of back-scattered light rather than sound [24,25]. By scanning the optical beam across tissue samples and measuring the back-scattered light as a function of axial depth and transverse location, OCT generates cross-sectional, tomographic images of surface tissue micro-structures. By scanning the optical beam across tissue samples and measuring the back-scattered light as a function of axial depth and transverse location, OCT obtains cross-sectional, tomographic images of surface tissue micro-structures. Stacking a series of 2D OCT images creates a 3D representation of tissue morphology [26,27], providing further insight into sample characteristics through polarized light analysis.

In this study, a combination of Mueller matrix OCT and deep learning was employed to quantitatively analyze the development of multiple zebrafish organs. Zebrafish images from 1-19 dpf were obtained using Mueller matrix OCT. Deep learning was then implemented to

automatically segment zebrafish organs, including embryos, eyes, yolk sac, and swim bladder. We calculated the volume of each organ and determined their developmental trends over 19 days. And then, we quantified the proportion of organs during zebrafish development. Our results demonstrated that although the development of the spine and swim bladder progressed relatively slower than other organs, the overall trend remained growth-oriented. Our findings indicate that the presented method accurately observes the development of various organs during zebrafish growth and provides a convenient and rapid approach for analyzing their morphological changes. This method may also serve as an auxiliary tool for monitoring anomalies during zebrafish development.

2. Materials and methods

2.1. Preparation and culture of zebrafish

The animal protocol in this study was approved by the Committee on Animal Care and Use at Fujian Normal University. Wild-type zebrafish were provided by the Zebrafish Resource Center. The laboratory rearing tank was maintained at a temperature of $28.5 \pm 1.0^\circ\text{C}$ and a hydrogen potential (pH) of 7.0 ± 0.2 . Zebrafish were kept in an environment with a 14-hour light and 10-hour dark photoperiod and had their water changed and were fed shrimp twice daily at 10 a.m. and 3 p.m. [28]. Four zebrafish embryonic development over the course of 19 days were observed by Mueller matrix OCT, starting from the first day after fertilization. The developmental process was divided into two developmental stages, the embryos stage and the larvae stage. In the setup of the experiment, 1-3 dpf was the embryos stage and 4-19 dpf was the larvae stage. In particular, embryo age of 1dpf refers to 0-24hpf, 2 dpf refers to 24-48 hpf, and 3dpf refers to 48-72 hpf, and more than 72 hpf refers to larva. Prior to image collection, zebrafish were anesthetized using a solution of 10 μl MS-222 with 15 ml water. After image collection, the zebrafish used in the experiment were transferred to clean water to recover and continue breeding.

2.2. Mueller matrix optical coherence tomography

A home-made spectral domain Mueller matrix OCT system employed in this study has been described in our previous work [27]. The axial and lateral resolutions of the system in air are 8.9 μm and 18.2 μm , respectively. By adding the sample attenuation constant, our system has a sensitivity of about 90 dB at surface, and a 24 dB drop was observed at about 1.5 mm below the surface. The depth of imaging is about 1 mm. The system has a maximum scanning range of 24 mm. The differences from the previous system are as follows: A polarization state generator (PSG, PG-001-13-FA/APC, Beijing Optical Application Co., LTD.) was integrated into our Mueller matrix OCT system to control the incident light's polarization state. A quarter-wave plate (QWP) with an angle of 22.5° to the horizontal plane in the fast axis direction is placed in front of reflected mirror. Polarized light is rotated 45° so that the horizontal and vertical polarization components of the reflected light have the same intensity. In addition, our system uses two spectrometers for simultaneous polarized light detection, enhancing data acquisition speed. The spectrometer integrates a CCD camera of 1300 nm band with 2048 pixels, and the maximum linear scanning speed reaches 76 kHz. The video acquisition card is connected with cameralink cable, and the grating resolution reaches 0.07 nm.

2.3. Zebrafish data acquisition

Polarization-difference-balanced-detection images of zebrafish were obtained using Mueller matrix OCT. This technique collected 400 cross-sectional images for each zebrafish, including both valid zebrafish structures and invalid environmental data. The lateral scanning field of view is adjusted with the growth of zebrafish in our experiment, and the maximum lateral scanning range is 24 mm. The lateral scanning field of view from 0 to 7dpf is 4 mm. After 7dpf, the field

of view changes to 6 mm. At the same time, a stereo microscope (Olympus-SZ61) equipped with a digital camera (microrome 6 usb3.0 camera) was used to observe and record the various stages of the zebrafish. In the data collection, the refractive index effect of sample was verified by slides. The refractive index was offset by proportional calculation to verify the validity of the data.

Depending on the vertical and horizontal incidence polarization states and the detected polarization state conditions, four different polarization state images can be obtained from each cross-section image. The four polarization state images can be labeled as $S_h D_h$, $S_h D_v$, $S_v D_h$, and $S_v D_v$, where S and D represent the sample and the detection arm, respectively, and subscripts h and v are horizontal and vertical line polarized light. From the four determined OCT images of polarization state, the four elements of the Mueller matrix M can be calculated as following [29]:

$$M_{00} = (S_h D_h + S_h D_v) + (S_v D_h + S_v D_v) \quad (1)$$

$$M_{01} = (S_h D_h + S_h D_v) - (S_v D_h + S_v D_v) \quad (2)$$

$$M_{10} = (S_h D_h - S_h D_v) + (S_v D_h - S_v D_v) \quad (3)$$

$$M_{11} = (S_h D_h - S_h D_v) - (S_v D_h - S_v D_v) \quad (4)$$

Figure 1 displays an image of the four elements of the Mueller matrix. To more accurately analyze the size and volume of zebrafish organs, the axial and lateral resolutions of Mueller matrix OCT images were adjusted to the same size. The differences in dispersion can be attributed to the disparate calculation methods applied on the two parameters. As M_{11} represents the polarization difference image and M_{00} signifies the total light intensity image, the images produced based on the respective computation methods of these parameters will inherently cause variation. Since organ segmentation requires a higher level of image detail, we evaluated the amount of image detail in different polarization states by comparing the region of interest (ROI) both inside and outside the organ boundaries of juvenile zebrafish. If the proportion of the inner and outer ROI regions is close to 1, the boundary difference between the two regions is small, indicating that the image contains less information. Our previous study [30] confirmed that the embryonic boundary of the M_{11} image is clearer than that of the M_{00} image, so M_{11} was selected to segment the yolk sac and embryo contour during the first three days of embryo development.

For smaller organs of juvenile zebrafish, the eye was taken as an example to analyze which polarization state image provides more detailed information, as shown in Fig. 2. In Fig. 2(a), the ROI region of inner and outer boundaries of the eye in the M_{00} image are labeled as ROI-I and ROI-II, respectively. $ProM_{00}$ denotes the area ratio of the inner and outer ROI region in M_{00} image's boundaries, expressed as $ProM_{00} = \frac{ROI-I}{ROI-II}$. Similarly, $ProM_{11}$ represents the area ratio of M_{11} , expressed as $ProM_{11} = \frac{ROI-III}{ROI-IV}$, as shown in Fig. 2(b). Figure 2(c) displays the average ratio results, with $ProM_{00}$ is about 0.5233 and $ProM_{11}$ is 0.6726. This suggests that the boundary distinction of smaller organs in the M_{00} image contains more detail than that of the M_{11} image. Therefore, M_{00} was employed for multi-organ segmentation of juvenile zebrafish during 4-19 dpf process.

2.4. Multi-classification of zebrafish organs using deep learning

To better visualize and analyze changes in organ structure during development, deep learning was employed to segment zebrafish organs. A total of 3,782 zebrafish images were collected over 19 days by Mueller matrix OCT, with 41 valid datasets. Among them, 350 datasets were manually labeled (as illustrated in Fig. 3), and these datasets were randomly divided into training datasets (90%) and validation datasets (10%) to enhance the model's robustness. The remaining images (unlabeled) served as prediction sets. It is worth noting that the training process was conducted on a computer with an i9-12900KF CPU, 128GB of memory, and an Nvidia RTX 4090 GPU. The U-Net network was chosen as the main trunk network, while ResNet50 was

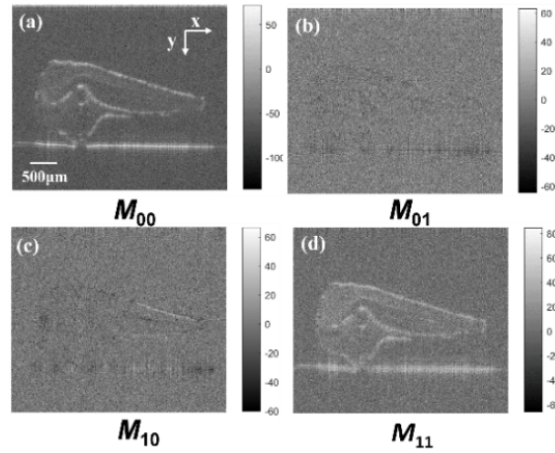


Fig. 1. Four elements of the Muller matrix M . (a) M_{00} ; (b) M_{01} ; (c) M_{10} ; (d) M_{11} , scalar bar is 500 μm .

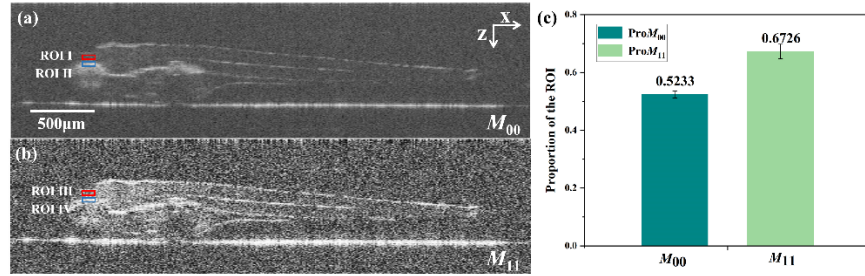


Fig. 2. Contrast analysis of ROIs in M_{00} and M_{11} . (a) M_{00} of zebrafish (the red box is ROI-I, the blue box is ROI-II); (b) M_{11} of zebrafish (the red box is ROI-III, the blue box is ROI-IV); (c) Proportion of the ROI between M_{00} and M_{11} . scalar bar is 500 μm .

selected as the backbone feature extraction network [31]. The batch size was set to 8, and the number of iterations to 300 based on our experimental environment. Additionally, the Adam optimizer was applied to optimize the model [32]. The learning rate was initially set to 0.0001 with a decay rate of 0.9995. Mean pixel accuracy (MPA) was utilized to assess classification accuracy. The formula for MPA is as follows [33]:

$$MPA = \frac{1}{C} \sum_i^C P_i \quad (5)$$

where C is the number of classes in the segmentation results, P_i is pixel accuracy for class i . The proportion of correct classification in the segmentation result was calculated by MPA, and then the average of this proportion is taken across all classes. MPA was measured every 5 batches. The higher the MPA, the more accurate the segmentation result.

2.5. Multi-classification volume quantification of zebrafish

2.5.1. Quantification of embryonic volume in zebrafish

The zebrafish embryo segmentation process is displayed in Fig. 4. First, zebrafish embryo data from 1dpf to 3dpf were collected by Mueller matrix OCT during this stage. Then, M_{11} images, as illustrated in Fig. 4(a), were taken to segment the zebrafish embryo outline and yolk sac structure.

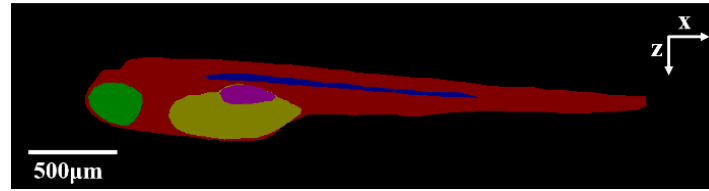


Fig. 3. Manual label image of zebrafish.

The segmented data was subsequently extracted to reconstruct a 3D image, as shown in Fig. 4(b). Next, the zebrafish embryonic outline and yolk sac were segmented, as displayed in Fig. 4(c) and (d). Finally, the contour volumes of the embryo and the yolk sac were calculated separately. The specific calculation method involves calculating the total pixel count for the embryo and the yolk sac in each M_{11} dataset. Each pixel was considered as an individual volume pixel. The x - z plane's actual area was determined by multiplying the axial resolution by the lateral resolution. The actual volume of zebrafish embryo segmentation data was calculated by multiplying the x - z plane area by the distance between images in the y direction.

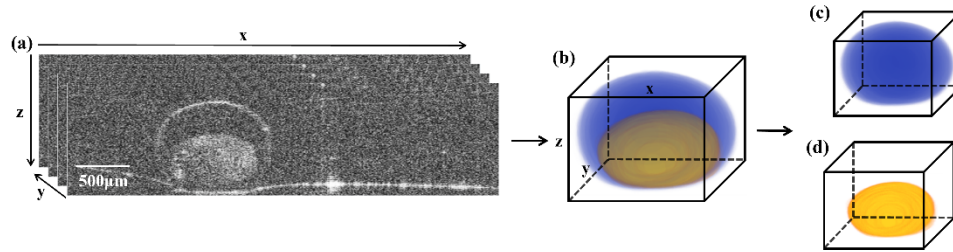


Fig. 4. Zebrafish embryo collection and segmentation process based on Mueller matrix OCT; (a) M_{11} images of zebrafish were collected by Mueller matrix OCT; (b) 3D zebrafish embryo; (c) Segmented 3D zebrafish embryo outline; (d) Segmented 3D zebrafish yolk sac.

2.5.2. Quantification of multi-organs volume in zebrafish

As zebrafish develop from embryos, their organs gradually form. This stage starts on the fourth day and ends on the nineteenth day. Figure 5(a) shows the cross-section of zebrafish collected at this stage. About 100 valid data (excluding invalid data) were collected to calculate the zebrafish organ volume for each zebrafish. To ensure uniform positioning during the collection process, zebrafish were placed in a lying position on the Mueller matrix OCT sample arm, as displayed in Fig. 5(b). Mueller matrix OCT's advantage is its ability to capture a more complete zebrafish structure compared to microscopic acquisition (Fig. 5(c)). Figure 5(b) displays a 3D reconstruction of a zebrafish data group, where 3D organs such as eyes, spine, and yolk sac can be clearly observed.

Organ volume was taken as a quantitative parameter to analyze zebrafish growth trends. The detailed calculation method of organ volume is as follows: First, the effective pixels of each B-scanned image were calculated, and the total number of effective pixels for a group of B-scanned images was added to obtain the complete zebrafish group's total pixel count. Each pixel was then considered as a cube. The actual volume could be calculated by $Volume = TP * LAR * LOR * D$, where TP is the zebrafish's total pixel count, LAR and LOR are the value of a single pixel point in the horizontal direction and axial direction in a B-scan image of Mueller matrix OCT system, respectively, and D is the actual distance between each image.

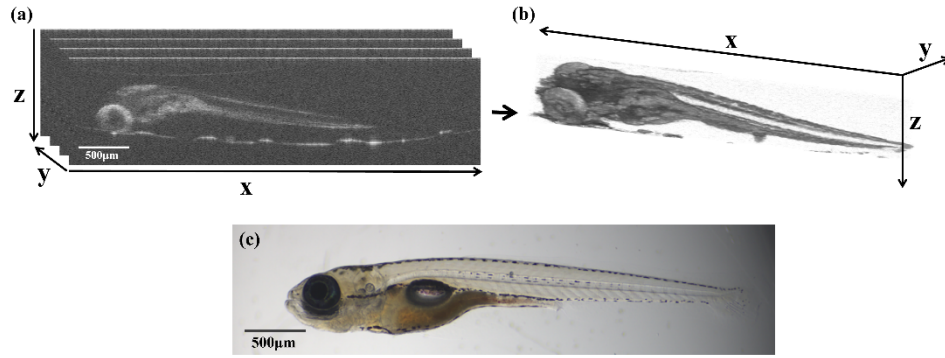


Fig. 5. Zebrafish images (a) zebrafish data collected by Mueller matrix OCT; (b) a 3D reconstruction of a zebrafish. (c) zebrafish by microscope.

2.6. Multi-classification proportion quantification method for zebrafish organs

To further analyze the zebrafish development process, the proportion of organs was calculated for quantitatively analyzing zebrafish developmental progress. For 1dpf-3dpf zebrafish embryos, the proportions of yolk sac volume to embryo outline volume by Mueller matrix OCT and yolk sac area to embryo outline area by microscope were calculated, respectively. The proportion expression is $P_{OCT} = \frac{V_{O-yolk}}{V_{O-embryo}}$ and $P_{micro} = \frac{S_{m-yolk}}{S_{m-embryo}}$, where P_{OCT} and P_{micro} represent the volume proportion and area proportion between the yolk and embryo outline by Mueller matrix OCT and microscope, respectively. V_{O-yolk} , S_{m-yolk} , $V_{O-embryo}$, and $S_{m-embryo}$ denote the volumes and areas of yolk sac and embryo outline by Mueller matrix OCT and microscope, respectively. For juvenile zebrafish (4dpf-19dpf), the proportions of eyes, spine, and yolk sac to the zebrafish body during 16 days were calculated using $P_1 = \frac{V_{eye}}{V_{body}}$, $P_2 = \frac{V_{spine}}{V_{body}}$, $P_3 = \frac{V_{yolk}}{V_{body}}$, and $P_4 = \frac{V_{swim}}{V_{body}}$, respectively.

2.7. Growth curve

Mathematical modeling has great potential to improve the understanding of biological development. Indeed, many models have successfully applied on the growth and development patterns of skin pigment cells and the formation of zebrafish stripes [34,35]. Logistic regression model was used for optimizing and estimating maximum likelihood estimation or gradient descent methods [36]. The model has strong explanatory power and has been widely used in biology, economics, ecology and other fields. The logistic equation is expressed as follows:

$$f(x) = \frac{L}{1 + e^{-k(x-x_0)}} \quad (6)$$

where, L denotes the maximum value, k is the slope, x represents time, and x_0 is the mean time. In this study, the logistic regression model was applied to fit and quantify the organs of zebrafish, so as to capture and analyze the development trend of each organ. In addition, we also used logistic function to fit and analyze the actual measured data of zebrafish growth, so as to evaluate the rationality of its development trend.

2.8. Data analysis

Data are expressed as mean \pm standard deviation. A two-sample t-test with unequal means was completed to determine whether the difference was significant in the statistical parameters between any two sample groups. Differences were regarded as statistically significant when $p < 0.05$.

3. Results

3.1. Segmentation of zebrafish organs based on deep learning

Deep learning was applied to segment and quantify the organs of zebrafish collected by Mueller matrix OCT. Throughout the training process, each batch required about 57 seconds. The entire training process took about 5 hours, 3 minutes and 26 seconds. It took about two minutes to extract a new set of organ data from zebrafish using trained model. The Dice-Loss function [37] was applied to address the imbalance problem of positive and negative data samples, as illustrated in Fig. 6(a). From the Figure, Dice-loss results in a noticeable oscillation in the loss curve's decline. The MPA score of this model is 92.34, as shown in Fig. 6(b).

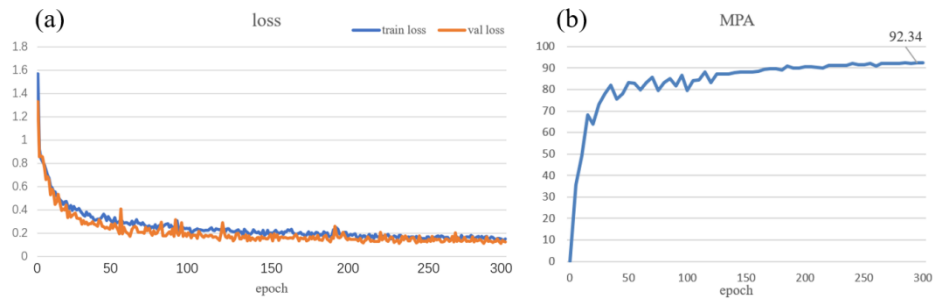


Fig. 6. (a) the loss decline curve of model training; (b) the evaluation curve of training MPA.

Using the trained model, five zebrafish organs, such as the body, eyes, spine, yolk sac, and swim bladder were successfully segmented. These segmentation results provide a basis for quantitative analysis of organ development in zebrafish.

Figure 7 displays the segmentation results of a single B-scan. We successfully segmented the body, eyes, spine, yolk sac, and swim bladder of the zebrafish. (a) is the entire zebrafish, while (b) to (f) show the body, eyes, spine, yolk sac, and swim bladder of the zebrafish, respectively. Following the principle of a complete organ count, we determined the volume of the zebrafish by summing the body, eyes, spine, yolk sac, and swim bladder volumes according to the multi-organ segmentation results of the single B-scan in Fig. 7. Similarly, we calculated the yolk sac volume by summing the yolk and swim bladder volumes.

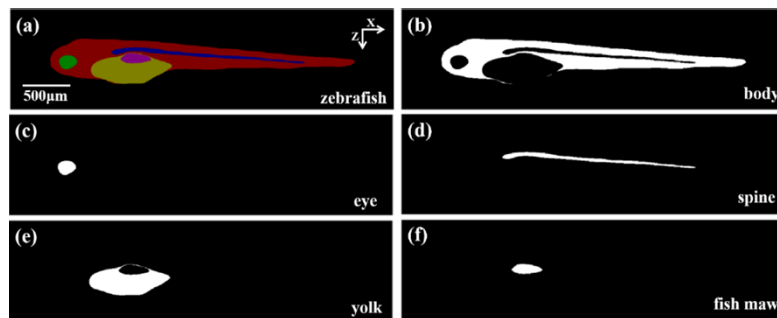


Fig. 7. Image of segmented zebrafish.

3.2. Developmental volume of zebrafish embryos

Figure 8 illustrates the images of zebrafish embryo development from 1 dpf to 3 dpf acquired by microscopy and Mueller matrix OCT. As seen in the figure, the embryo outline and yolk sac areas decrease over time, with a significant decrease observed on the third day. Additionally, the eyes and spine are clearly growing in Fig. 8(c) and (f).

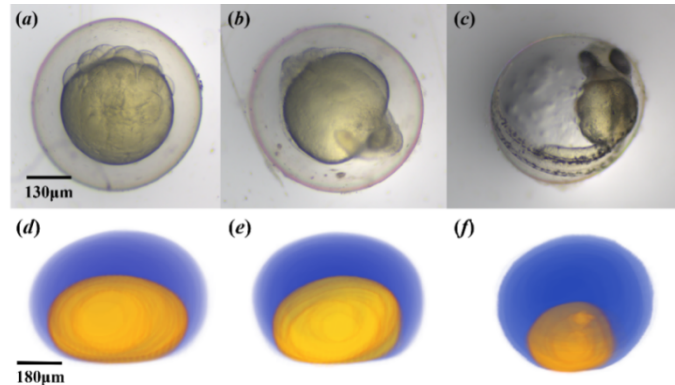


Fig. 8. Images of zebrafish during 1-3 days post-fertilization (dpf). (a)-(c) Images from microscopy; (d)-(f) Three-dimensional segmented images by Mueller matrix OCT.

Figure 9(a) and (b) are the area of the embryo and yolk sac obtained by microscopy and Mueller matrix OCT, separately. While Fig. 9(c) displays the volume of the embryo and yolk sac from 1 dpf to 3 dpf development measured by Mueller matrix OCT. The area of the embryo increases on the third day of development according to Fig. 9(a), which is inconsistent with our observations in Fig. 8. And in Fig. 9(b), the area of zebrafish embryos measured by Mueller matrix OCT is showing a gradual decreasing trend in the first three days of development, which is consistent with Fig. 8. The same decreasing trend is shown in Fig. 9(c), which is consistent with the actual embryonic developmental trend [38,39].

Furthermore, the proportion of yolk sac to embryo volume obtained by Mueller matrix OCT and area proportion obtained by microscopy were quantified and shown in Fig. 9(d). From the figure, the overall embryonic development trend exhibits a gradual decline, conforming to the general developmental pattern [38]. These outcomes affirm the feasibility of our quantitative method.

3.3. Developmental volume of zebrafish organs

Figure 10 illustrates the images of zebrafish development with 4, 10, 12 and 16 dpf acquired by Mueller matrix OCT, respectively. As seen in the figure, the size of zebrafish increase over time.

Figure 11 displays the quantitatively calculated volumes of zebrafish during the developmental process. This representation enables a more intuitive and clear analysis of zebrafish organ development during the 4-19 dpf stage.

We separately calculated the volume of three zebrafish organs: the swim bladder, eyes, and spine, as demonstrated in Fig. 11(b). From Fig. 11(b), it can be seen that the development of the spine stabilizes within 16 days, while the development of the eyes exhibits a noticeable upward trend. The swim bladder's volume fluctuates and is unstable during the growth process.

Figure 12 shows the volume development trend of yolk sac of zebrafish. The yolk sac is divided into two stages for statistics because the development of yolk sac is metabolic in the first few days, and then grow gradually after the fifth day. As can be seen from Fig. 12 (a), the volume

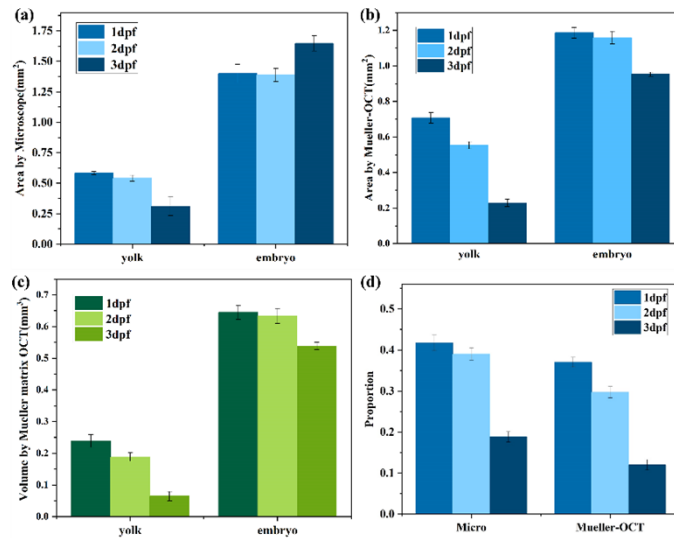


Fig. 9. Size of zebrafish yolk and embryo. (a) the area of embryonic development calculated by microscope; (b) the area of embryonic development calculated by Mueller matrix OCT; (c) development of volume area data of embryo and yolk sac in 1dpf-3dpf by Mueller matrix OCT; (d) Proportion between yolk sac volume and embryo.

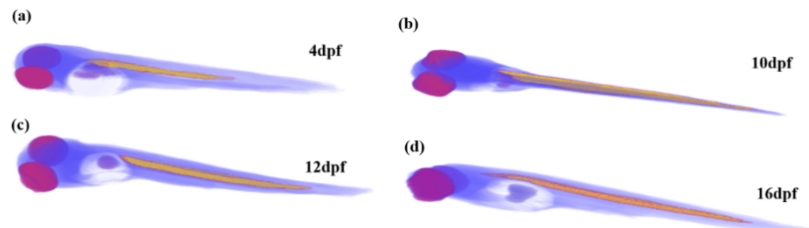


Fig. 10. Images of zebrafish during 4-16 days post-fertilization (dpf).

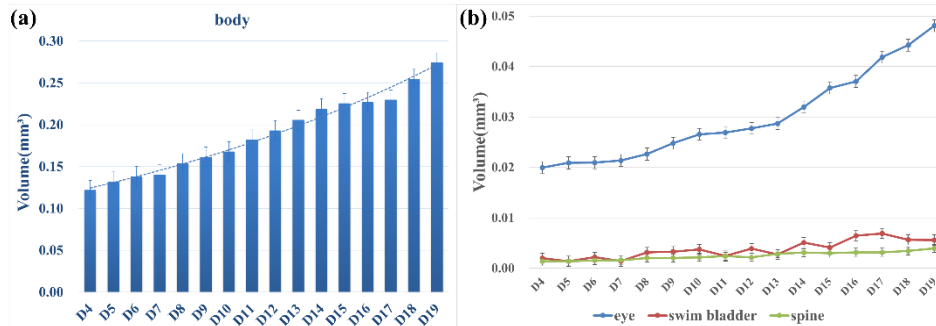


Fig. 11. Quantification of the volume of zebrafish (a) body; (b) multiple organs

of yolk sac decreased rapidly in the first 4 days, stabilized at 4-7 days, and gradually developed at 8-19 days, as shown in Fig. 12 (b).

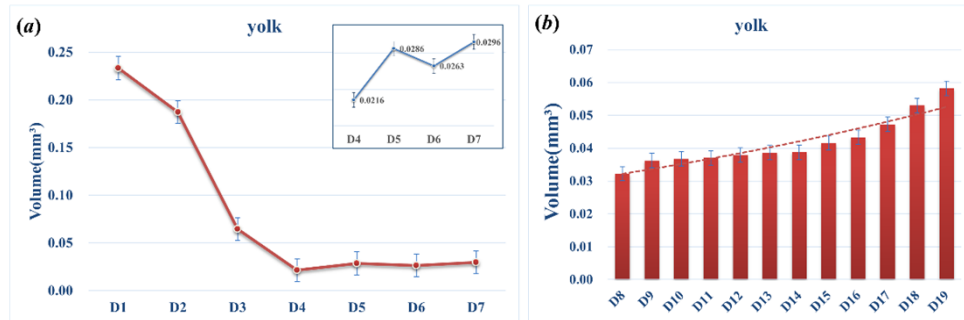


Fig. 12. Volume analysis of yolk sac of zebrafish by Mueller matrix OCT. (a) Line plots of yolk sac development in 1-7 dpf; (b) Bar chart of yolk sac development in 8-19 dpf.

Similar to our examination of zebrafish embryos in the previous section, the growth data of zebrafish organs by quantifying the proportion of each organ were analyzed. Figure 13 presents the proportion of the eyes, spine, yolk, and swim bladder volumes to the zebrafish body development volume at each developmental time point, represented by P_1 , P_2 , P_3 , P_4 (description in section 2.6). In Fig. 13, P_3 value also reflects the yolk sac volume fluctuation caused by zebrafish feeding at 5 dpf. The P_2 and P_4 curves exhibit no apparent changes relative to their absolute volumes because these organs are relatively small in size, fluctuating between 1% and 2% compared to the body, consequently stabilizing the proportion data.

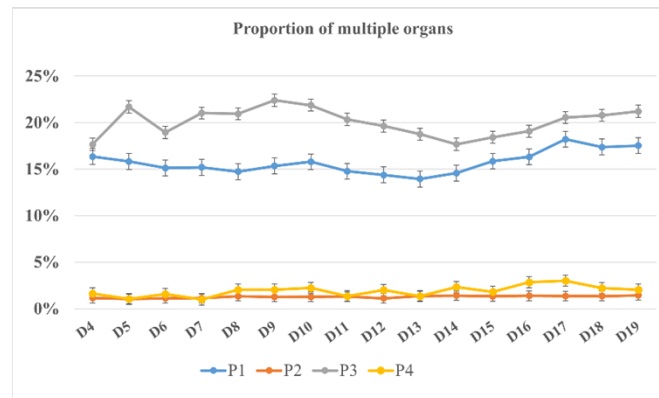


Fig. 13. Proportion of multiple organs.

3.4. Mathematical model of zebrafish organs development

Logistic function was employed to fit the data of multiple organs of zebrafish to confirm the feasibility of our method and the reliability of the result [40]. Excluding the body volume and 1-7 dpf yolk volume, we uniformly adjusted the maximum ordinate of the organ development fitting curve to 0.06 mm^3 for a unified observation. Figure 14 displays the logistic function fitting results of the zebrafish multi-organ volume data. As seen in Fig. 14(a) and (b), the fitting results reveal that the actual volume of the zebrafish body and eyes displays well with the theoretical data. These fitting outcomes also confirm the validity of the body and eye data statistics in Section 3.3.

As shown in Fig. 14(c) and (d), the spine and swim bladder exhibit a subtle increase in fitting, which is consistent with the statistics in Fig. 11(b).

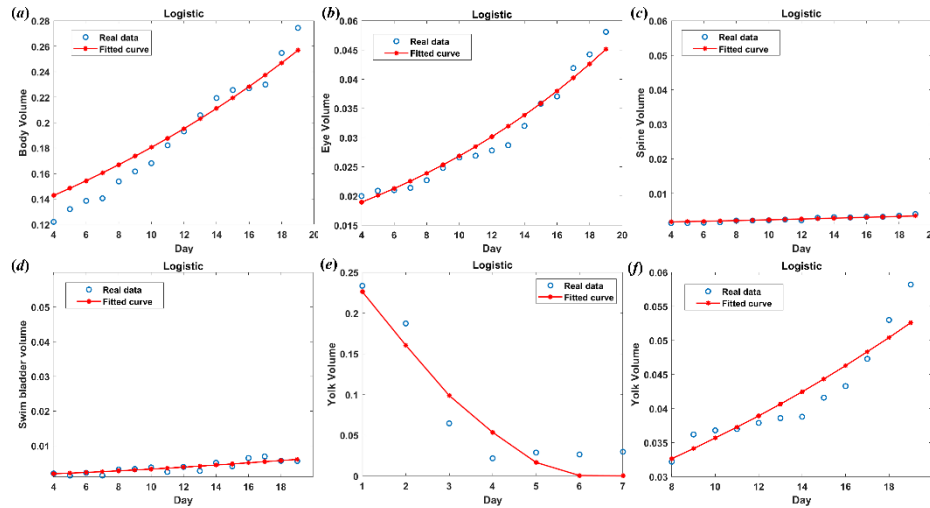


Fig. 14. Logistic fitting curve of multiple organ volume of zebrafish. (a) body volume fitting of zebrafish; (b) Eye volume fitting of zebrafish; (c) Spine volume fitting of zebrafish; (d) Swim bladder volume fitting of zebrafish; (e) and (f) Yolk sac volume fitting of zebrafish during 1-7dpf and 8-19dpf respectively.

Because the volume analysis of yolk sac was divided into two stages, the logistic fitting of its volume was also performed in two stages. Figure 14(e) and (f) exhibit the yolk sac degradation fitting within the first seven days of development and growth with external food absorption after seven days, respectively. As shown in Fig. 14, the multi-organ fitting curve is consistent with the experimental results, reflecting our experiment's effectiveness.

4. Discussion

Unlike light and fluorescent imaging technology, OCT is a non-invasive imaging technique that can be useful for imaging adult zebrafish and tracking disease progression or drug effects in longitudinal studies [41,42]. Compared with conventional OCT, Mueller matrix OCT works by assessing the polarization state of the scattered light. It eliminates the need for manual waveplate adjustments during deflection, resulting in more precise polarization states. Mueller matrix OCT enables quantitative analysis of tissue birefringence, which can provide information on tissue structure and functional imaging. For example, M_{00} and M_{11} could be calculated from the Mueller matrix OCT. In our study, Mueller matrix OCT combined with deep learning was used to quantitatively analyze the development of multiple organs in zebrafish. By using Mueller matrix OCT, the polarization images of zebrafish from 1-19dpf can be obtained, with high information content.

To the best of our knowledge, the size of zebrafish embryo is generally estimated by the length or diameter of the embryo from microscope, while the volume of the embryo is obtained by using the diameter to estimate the volume of the embryo as a sphere [43,44]. It is known that the embryo diameter is 0.4-0.7 mm diameter on the 1dpf according to the zebrafish embryo stage development, corresponding to a volume of about 0.03-0.41 mm³ [38]. It is particularly important to monitoring the volume when zebrafish has abnormalities or lesions in the z direction. From the microscope, volume monitoring can only be obtained by moving the zebrafish and imaging it multiple times. This will cause measurement errors, and time consuming. The quantitative

characterization of zebrafish multi-organ volume based on Mueller matrix OCT solves these problems effectively. In this study, the organ volume of zebrafish from 1dpf to 19dpf was quantified, and the volume development and growth curve was generated. The results show that the growth of various organs during the development of zebrafish can reflect the developmental characteristics of each stage more completely and precisely through the volume. By comparing Fig. 9 (a) and Fig. 9 (b), the areas calculated using Mueller matrix OCT measurements appear to be more consistent with morphological developmental trends than those using microscopic measurements based on the analysis of the normal trend of zebrafish embryo development [39,45]. In addition, the data obtained by Mueller matrix OCT can be quantified and analyzed from the volume perspective of the embryo development trends, providing a more reliable and intuitive perspective for the quantification of embryonic volume.

From Fig. 11(a), it can be observed that the volume development of zebrafish organs demonstrates a steadily increasing trend. This growth pattern is consistent with the typical growth of zebrafish under normal feeding conditions [39,46]. From Fig. 11(b), it can be seen that the development of the spine stabilizes within 16 days, while the development of the eyes exhibits a noticeable upward trend. The swim bladder's volume fluctuates and is unstable during the growth process. As fish use the swim bladder to maintain balance in water, the organ contracts and expands its smooth muscles and striated muscles to control gas volume in the water based on depth. Smooth muscles, striated muscles, and blood vessels play a key role in the flow of gas to and from the swim bladder [47]. So, the swim bladder's size fluctuates as it grows. As shown in Fig. 11(b), the minimum (4 dpf) and maximum (19 dpf) fish swim bladder values are $2.0 \times 10^{-3} \text{ mm}^3$ and $5.6 \times 10^{-3} \text{ mm}^3$, respectively. In Fig. 13, the percentage of P_2 and P_4 for the spine and swim bladder fluctuate between 1% and 2%. The comparison of the volume between 4 dpf and 19 dpf reveals that the swim bladder volume gradually increases during 16 days of growth, even considering factors that affect the organ's contraction and expansion.

Figure 12 (a) shows the yolk sac volume increase on the fifth day, while fluctuations occur due to the sudden intervention of exogenous feeding. The yolk sac is an important nutrient supply source in the development stage of 1-7dpf, and it is usually gradually absorbed. For the first five days, the yolk sac is the only source of nutrients. Beginning on the fifth day, external nutrition is supplemented, and at this time, the yolk sac is not completely consumed. Thus, this stage presents both endogenous and exogenous nutrients. From the seventh day, nutrition absorption is mainly dependent on external feeding [48,49]. The volume of yolk sac increased linearly, as shown in Fig. 12 (b).

Muller matrix OCT combined with deep learning was used to obtain polarization images during the 1-19 dpf process of zebrafish development in our study. The organs were then segmented to obtain the volume, and the volume growth index was further analyzed. Results provides an effective means to monitor the development of zebrafish. Actually, Segmentation of zebrafish organs may pose challenges due to the high complexity of organ morphology and the different developmental stages involved [50]. For one thing, the small size of zebrafish embryos makes it difficult to accurately segment internal organs, especially if the organs are close to each other. This requires careful imaging and analysis to separate and segment individual organs with minimal overlap or misclassification. Then, zebrafish embryos undergo rapid and complex developmental changes, which poses challenges for accurate organ segmentation. The morphology and location of organs can change rapidly over time, making it necessary to use imaging techniques with high temporal resolution to capture these changes [16]. Additionally, Muller matrix OCT also has its limitations in zebrafish imaging compared with traditional OCT [51]. The limitations of Mueller matrix OCT include its complexity, slow imaging speed, limited availability, and high cost. Mueller matrix OCT is a more complex imaging technique than traditional OCT, which can make it challenging to use and limit its widespread adoption. Additionally, Mueller matrix OCT is typically slower than traditional OCT, making it less suitable for imaging dynamic biological

processes. However, Mueller matrix OCT also has unique prospects due to its ability to extract more detailed information about the polarization properties of the imaged tissue. This can enable more complex characterization of biological tissues at the microscale, leading to new clinical and research applications.

5. Conclusion

In this paper, we proposed a multi-classification analysis method for zebrafish organs by combining deep learning and Mueller matrix OCT. By utilizing Mueller matrix OCT, we quantified the volume and growth trends of zebrafish organs from a 3D perspective. We also quantified the proportion of select organs. Our results demonstrate that the general growth trend of zebrafish increases gradually within 16 days. Although spine development is slow, it confirms the stable growth trend with subtle changes. Finally, we used the logistic function to fit the data of zebrafish multi-organs to confirm our method's feasibility. The logistic function fitting results further demonstrate the feasibility of the Mueller matrix OCT method in analyzing the growth and developmental trends of zebrafish multi-organs.

Although the study is on a small number of samples, these results indicate that the organs volume and growth trend of zebrafish during the development process. It can provide more abundant analytical means for toxicology, developmental biology and other disciplines in the analysis of organ developmental malformations.

Funding. National Natural Science Foundation of China (61875038, 81901787).

Acknowledgement. We acknowledge the support of National Natural Science Foundation of China and Special Funds of the Central Government Guiding Local Science and Technology Development.

Disclosures. The authors declare that there are no conflicts of interest related to this article.

Data availability. Data underlying the results presented in this paper are not publicly available at this time but may be obtained from the authors upon reasonable request. Codes used in this paper are available from Ref [52].

References

1. R. Feldman and A. I. Eidelman, "Biological and environmental initial conditions shape the trajectories of cognitive and social-emotional development across the first years of life," *Dev Sci.* **12**(1), 194–200 (2009).
2. S. A. Brittin, S. J. Duivestijn, M. Belmamoune, L. F. Bertens, and W. Bitter, "Zebrafish development and regeneration: new tools for biomedical research," *Int J Dev Biol.* **53**(5-6), 835–850 (2009).
3. J. Giacomotto and L. Segalat, "High-throughput screening and small animal models, where are we?" *Br J Pharmacol.* **160**(2), 204–216 (2010).
4. K. Howe, M. D. Clark, C. F. Torroja, J. Torrance, C. Berthelot, M. Muffato, J. E. Collins, S. Humphray, K. McLaren, and L. Matthews, "The zebrafish reference genome sequence and its relationship to the human genome," *Nature* **496**(7446), 498–503 (2013).
5. F. Tonelli, J. W. Bek, R. Besio, A. De Clercq, L. Leoni, P. Salmon, P. J. Coucke, A. Willaert, and A. Forlino, "Zebrafish: A Resourceful Vertebrate Model to Investigate Skeletal Disorders," *Front. Endocrinol.* **11**, 489 (2020).
6. K. Dooley and L. I. Zon, "Zebrafish: a model system for the study of human disease," *Curr Opin Genet Dev.* **10**(3), 252–256 (2000).
7. M. R. Riddle and C. K. Hu, "Fish models for investigating nutritional regulation of embryonic development," *Dev Biol* **476**, 101–111 (2021).
8. X. Han, B. Wang, D. Jin, K. Liu, H. Wang, L. Chen, and Y. Zu, "Precise dose of folic acid supplementation is essential for embryonic heart development in Zebrafish," *Biology* **11**(1), 28 (2021).
9. W. Huang, T. Wu, W. W. Au, and K. Wu, "Impact of environmental chemicals on craniofacial skeletal development: Insights from investigations using zebrafish embryos," *Environ Pollut.* **286**, 117541 (2021).
10. L. Qian, J. Liu, Z. Lin, X. Chen, L. Yuan, G. Shen, W. Yang, D. Wang, Y. Huang, S. Pang, X. Mu, C. Wang, and Y. Li, "Evaluation of the spinal effects of phthalates in a zebrafish embryo assay," *Chemosphere* **249**, 126144 (2020).
11. J. Zhang, Y. Wang, J. Liu, Z. Tang, and Z. Wang, "Multiple organ-specific cancers classification from PET/CT images using deep learning," *Multimed Tools Appl.* **81**(12), 16133–16154 (2022).
12. Z. Liu, S. Wang, D. Dong, J. Wei, C. Fang, X. Zhou, K. Sun, L. Li, B. Li, M. Wang, and J. Tian, "The applications of radiomics in precision diagnosis and treatment of oncology: opportunities and challenges," *Theranostics* **9**(5), 1303–1322 (2019).
13. T. Higaki, Y. Nakamura, J. Zhou, Z. Yu, T. Nemoto, F. Tatsugami, and K. Awai, "Deep learning reconstruction at CT: phantom study of the image characteristics," *Acad Radiol.* **27**(1), 82–87 (2020).

14. M. Zvolský, M. Schaar, S. Seeger, S. Rakers, and M. Rafecas, "Development of a digital zebrafish phantom and its application to dedicated small-fish PET," *Phys. Med. Biol.* **67**(17), 175005 (2022).
15. Y. Z. Zhang, Y. C. Ouyang, Y. Hou, H. Schatten, D. Y. Chen, and Q. Y. Sun, "Mitochondrial behavior during oogenesis in zebrafish: a confocal microscopy analysis," *Dev Growth Differ.* **50**(3), 189–201 (2008).
16. B. Zhang, K. E. Pas, T. Ijaseun, H. Cao, P. Fei, and J. Lee, "Automatic segmentation and cardiac mechanics analysis of evolving zebrafish using deep learning," *Front Cardiovasc Med.* **8**, 675291 (2021).
17. V. H. C. de Albuquerque, D. d. A. Rodrigues, R. F. Ivo, S. A. Peixoto, T. Han, W. Wu, and P. P. Rebouças Filho, "Fast fully automatic heart fat segmentation in computed tomography datasets," *Comput Med Imag Grap.* **80**, 101674 (2020).
18. J. Dong, J. Fu, and Z. He, "A deep learning reconstruction framework for X-ray computed tomography with incomplete data," *PLoS One* **14**(11), e0224426 (2019).
19. P. J. Keller, A. D. Schmidt, J. Wittbrodt, and E. H. Stelzer, "Digital scanned laser light-sheet fluorescence microscopy (DSLM) of zebrafish and Drosophila embryonic development," *Cold Spring Harb Protoc.* **2011**(10), pdb.prot065839 (2011).
20. P. A. Santi, "Light sheet fluorescence microscopy: a review," *J Histochem Cytochem.* **59**(2), 129–138 (2011).
21. J. Yin, G. Yang, X. Qin, H. Li, and L. Wang, "Optimized U-Net model for 3D light-sheet image segmentation of zebrafish trunk vessels," *Biomed. Opt. Express* **13**(5), 2896–2908 (2022).
22. S. Aumann, S. Donner, J. Fischer, and F. Müller, "Optical coherence tomography (OCT): principle and technical realization," *High Resolution Imaging in Microscopy and Ophthalmology* 59–85 (2019).
23. A. F. Fercher, "Optical coherence tomography—development, principles, applications," *Z Med Phys.* **20**(4), 251–276 (2010).
24. A. G. Podoleanu, "Optical coherence tomography," *Brit J Radiol.* **78**(935), 976–988 (2005).
25. J. G. Fujimoto, "Optical coherence tomography for ultrahigh resolution in vivo imaging," *Nat. Biotechnol.* **21**(11), 1361–1367 (2003).
26. M. L. Gabriele, G. Wollstein, H. Ishikawa, J. Xu, J. Kim, L. Kagemann, L. S. Folio, and J. S. Schuman, "Three dimensional optical coherence tomography imaging: advantages and advances," *Prog Retin Eye Res.* **29**(6), 556–579 (2010).
27. D. Li, Z. Li, J. Zhang, K. Li, S. Wu, Y. He, and Y. Lin, "Orthogonal-polarization-gating optical coherence tomography for human sweat ducts in vivo," *J. Biophotonics* **14**(4), e202000432 (2021).
28. B. Tsang, H. Zahid, R. Ansari, R. C.-Y. Lee, A. Partap, and R. Gerlai, "Breeding zebrafish: a review of different methods and a discussion on standardization," *Zebrafish* **14**(6), 561–573 (2017).
29. G. Yao and L. V. Wang, "Two-dimensional depth-resolved Mueller matrix characterization of biological tissue by optical coherence tomography," *Opt. Lett.* **24**(8), 537–539 (1999).
30. K. Li, Y. Wang, Y. Liu, W. Li, Z. Weng, H. Li, Y. He, and Z. Li, "Morphological characteristics of zebrafish's yolk sac for malformation based on orthogonal-polarization-gating optical coherence tomography," *J. Biophotonics* **15**(10), e202200098 (2022).
31. Z. Zhou, M. M. Rahman Siddiquee, N. Tajbakhsh, and J. Liang, "Unet++: A nested u-net architecture for medical image segmentation," *Deep Learn Med Image Anal Multimodal Learn Clin Decis Support.* **11045**, 3–11 (2018).
32. Y. Zhou, M. Zhang, J. Zhu, R. Zheng, and Q. Wu, "A randomized block-coordinate adam online learning optimization algorithm," *Neural Comput Appl.* **32**(16), 12671–12684 (2020).
33. S. Li, X. Zhao, and G. Zhou, "Automatic pixel-level multiple damage detection of concrete structure using fully convolutional network," *Comput-Aided Civ Inf.* **34**(7), 616–634 (2019).
34. M. R. McGuirl, A. Volkening, and B. Sandstede, "Topological data analysis of zebrafish patterns," *Proc. Natl. Acad. Sci. U. S. A.* **117**(10), 5113–5124 (2020).
35. Y. Zhu, G. Su, D. Yang, Y. Zhang, L. Yu, Y. Li, J. P. Giesy, R. J. Letcher, and C. Liu, "Time-dependent inhibitory effects of Tris(1, 3-dichloro-2-propyl) phosphate on growth and transcription of genes involved in the GH/IGF axis, but not the HPT axis, in female zebrafish," *Environ Pollut.* **229**, 470–478 (2017).
36. P. F. Verhulst, "Notice sur la loi que la population suit dans son accroissement," *J. Biological Phys.* **3**(4), 183–192 (1975).
37. X. Li, X. Sun, Y. Meng, J. Liang, F. Wu, and J. Li, "Dice loss for data-imbalanced NLP tasks," *arXiv*, arXiv.1911.02855 (2019).
38. C. B. Kimmel, W. W. Ballard, S. R. Kimmel, B. Ullmann, and T. F. Schilling, "Stages of embryonic development of the zebrafish," *Dev Dynam.* **203**(3), 253–310 (1995).
39. U. Strahle, S. Scholz, R. Geisler, P. Greiner, H. Hollert, S. Rastegar, A. Schumacher, I. Selderslaghs, C. Weiss, H. Witters, and T. Braunbeck, "Zebrafish embryos as an alternative to animal experiments—a commentary on the definition of the onset of protected life stages in animal welfare regulations," *Reprod. Toxicol.* **33**(2), 128–132 (2012).
40. A. V. Schwartz, K. E. Sant, J. Navarrete, and U. Z. George, "Mathematical modeling of the interaction between yolk utilization and fish growth in zebrafish, *Danio rerio*," *Development* **148**(9), dev193508 (2021).
41. T. J. Bailey, D. H. Davis, J. E. Vance, and D. R. Hyde, "Spectral-domain optical coherence tomography as a noninvasive method to assess damaged and regenerating adult zebrafish retinas," *Invest. Ophthalmol. Vis. Sci.* **53**(6), 3126–3138 (2012).

42. A. Lichtenegger, P. Mukherjee, J. Tamaoki, L. Bian, L. Zhu, I. Abd El-Sadek, S. Makita, K. Leskovar, M. Kobayashi, B. Baumann, and Y. Yasuno, "Multicontrast investigation of in vivo wildtype zebrafish in three development stages using polarization-sensitive optical coherence tomography," *J. Biomed. Opt.* **27**(01), 016001 (2022).
43. S. Augustine, B. Gagnaire, M. Floriani, C. Adam-Guillermine, and S. A. Kooijman, "Developmental energetics of zebrafish, *Danio rerio*," *Comp Biochem Physiol A Mol Integr Physiol.* **159**(3), 275–283 (2011).
44. C. Singleman and N. G. Holtzman, "Growth and maturation in the zebrafish, *Danio rerio*: a staging tool for teaching and research," *Zebrafish* **11**(4), 396–406 (2014).
45. S. Ali, D. L. Champagne, H. P. Spaink, and M. K. Richardson, "Zebrafish embryos and larvae: a new generation of disease models and drug screens," *Birth Defects Res C.* **93**(2), 115–133 (2011).
46. A. T. McCurley and G. V. Callard, "Characterization of housekeeping genes in zebrafish: male-female differences and effects of tissue type, developmental stage and chemical treatment," *BMC Mol Biol.* **9**(1), 102 (2008).
47. J. L. Finney, G. N. Robertson, C. A. McGee, F. M. Smith, and R. P. Croll, "Structure and autonomic innervation of the swim bladder in the zebrafish (*Danio rerio*)," *J Comp Neurol.* **495**(5), 587–606 (2006).
48. D. Fraher, A. Sanigorski, N. A. Mellett, P. J. Meikle, A. J. Sinclair, and Y. Gibert, "Zebrafish embryonic lipidomic analysis reveals that the yolk cell is metabolically active in processing lipid," *Cell Rep.* **14**(6), 1317–1329 (2016).
49. C. Wilson, "Aspects of larval rearing," *ILAR J.* **53**(2), 169–178 (2012).
50. E. C. Kugler, J. Frost, V. Silva, K. Plant, K. Chhabria, T. J. A. Chico, and P. A. Armitage, "Zebrafish vascular quantification: a tool for quantification of three-dimensional zebrafish cerebrovascular architecture by automated image analysis," *Development* **149**(3), 3 (2022).
51. A. Lichtenegger, B. Baumann, and Y. Yasuno, "Optical coherence tomography is a promising tool for zebrafish-based research-a review," *Bioengineering* **10**(1), 5 (2022).
52. K. Li, B. Liu, Z. Wang, Y. Li, H. Li, S. Wu, and Z. Li, "Quantitative characterization of zebrafish development based on multiple classifications using Mueller matrix OCT," Fujian Normal University, Github, 2023, <https://github.com/Binbuilding/zebrafish>.